Measurement of the sound velocity and Grüneisen parameter of polystyrene at inertial confinement fusion conditions

C. A. McCoy [1,*] S. X. Hu [2] M. C. Marshall,[2] D. N. Polsin,[2] D. E. Fratanduono,[3] Y. H. Ding,[2]
P. M. Celliers [3] T. R. Boehly,[2] and D. D. Meyerhofer [4]

[1]*Sandia National Laboratories, Albuquerque, New Mexico 87185, USA*
[2]*Laboratory for Laser Energetics, University of Rochester, Rochester, New York 14263, USA*
[3]*Lawrence Livermore National Laboratory, Livermore, California 94550, USA*
[4]*Los Alamos National Laboratory, Los Alamos, New Mexico 87545, USA*

The principal Hugoniot, sound velocity, and Grüneisen parameter of polystyrene were measured at conditions relevant to shocks in inertial confinement fusion implosions, from 100 to 1000 GPa. The sound velocity is in good agreement with quantum molecular dynamics calculations and all tabular equation of state models at pressures below 200 GPa. Above 200 GPa, the experimental results agree with two of the examined tables, but do not agree with the most recent table developed for design of inertial confinement fusion (ICF) experiments. The Grüneisen parameter increases with density below $\sim 3.1\,\mathrm{g/cm^3}$ and approaches the asymptotic value for an ideal gas after complete dissociation. This behavior is in good agreement with quantum molecular dynamics results and previous work but is not represented by any of the tabular models. The discrepancy between tabular models and experimental measurement of the sound velocity and Grüneisen parameter is sufficient to impact simulations of ICF experiments.

I. INTRODUCTION

Laser-driven inertial confinement fusion (ICF) experiments implode spherical capsules of an ablator material filled with deuterium-tritium (DT) fuel that is compressed to conditions sufficient to support thermonuclear burn [1]. Optimizing these implosions requires a trade-off between stability and performance. The favored drive profiles use a series of shockwaves to approximate an isentropic compression path while providing discrete events that enable control of the capsule adiabat as it is compressed. Drives having three initial shocks followed by a large compression wave are experimentally manageable and produce satisfactory results [2]. These shocks transit the ablator in a precisely timed sequence producing single-, double-, and triple-shocked states which are further compressed to extreme conditions [3,4]. To design and simulate these implosions, it is essential that the equation of state (EOS) of the ablator be accurately known [5].

For these studies, one needs the principal Hugoniot and sound velocity in the shocked material, as well as the multiply shocked and release behaviors. With knowledge of the Grüneisen parameter, which can be calculated from the Hugoniot and sound velocity, the off-Hugoniot behavior of the ablator can be calculated using a model (i.e., Mie-Grüneisen EOS) in the absence of phase transitions [6]. This is necessary to model the propagation of subsequent shocks through the ablator and to determine the release state at the ablator-fuel interface [7]. This release state determines the pressure transmitted into the fuel, thereby setting the fuel adiabat.

Knowledge of the sound velocity provides insight into the growth of hydrodynamic instabilities [8–12] and shock timing [3,4]. The growth of hydrodynamic instabilities can degrade implosion performance and prevent achievement of ignition. In particular, the ablative Richtmyer-Meshkov (RM) instability determines the perturbation seed for the Rayleigh-Taylor (RT) instability whose growth is the most damaging to implosion performance [8,10].

Common ablator materials include plastics [2,13] (primarily glow discharge polymer, GDP), high-density carbon [14], and beryllium [15]. Recent developments in the fabrication of cross-linked polystyrene (CH) capsules for direct-drive fusion have indicated that fewer surface defects are present than in the GDP capsules, which could lead to the extensive use of CH capsules for ICF experiments [16]. Additionally, CH has commonly been used as a surrogate for GDP due to its similar hydrodynamic response and more reproducible fabrication process [17–19].

The polystyrene Hugoniot has previously been determined in the 100–1000 GPa range using single- [17,20,21] and double-shock [17] experiments and in the 2500–6000-GPa range using converging shocks [22]. Additional plastic Hugoniot data have been measured for polyethylene [17], polymethylpentene [23], GDP [13,24], and doped GDP [13,25,26]. Quantum molecular dynamics (QMD) calculations have expanded the understanding of high-pressure behavior and provided details on the role played by chemical composition, dissociation, ionization, and electron degeneracy on thermodynamic properties at extreme conditions [18,19,27–29].

We present measurements of the principal Hugoniot, sound velocity, and Grüneisen parameter of polystyrene from 100

*camccoy@sandia.gov

to 850 GPa. These results supplement existing data for the polystyrene Hugoniot over the pressure range relevant to the first and second shocks in an ICF implosion. The sound velocity and Grüneisen parameter data enable calibration of off-Hugoniot parameters and will support further development of wide-ranging EOS models for ICF ablator materials. We also present QMD calculations of the sound velocity and Grüneisen parameter which account for dissociation over this range of pressures. Both the experimental and QMD results exhibit a decrease in Grüneisen parameter at decreasing densities approaching melting along the Hugoniot.

This paper is organized as follows: Sections II and III describe the methods used to carry out the experiments and QMD calculations, respectively. In Sec. IV, we present the analysis techniques used to extract the Hugoniot and sound velocity from the raw data. The results and a discussion on their implications for EOS modeling and ICF experiments are given in Sec. V. Finally, Sec. VI summarizes the findings and the general conclusions from this study.

II. EXPERIMENTAL METHOD

Experiments to measure the shocked sound velocity of CH were conducted at the OMEGA EP laser facility at the University of Rochester's Laboratory for Laser Energetics [30]. Two beams of the frequency-tripled Nd:glass laser operating at 351 nm were used to drive shocks into multilayered targets. The laser intensity ranged from ~0.06 to 1.1×10^{14} W/cm^2 for pulse durations of either 4 or 6 ns. The laser spots were smoothed using distributed phase plates [31] with planar regions 1100 μm in diameter.

The targets were nominally 60 μm thick, 3-mm × 3-mm flat *z*-cut, α-quartz baseplates [Fig. 1(a)]. Deposited to the front (laser side) of the baseplate was a 15–20-μm-thick Parylene-N layer to serve as a low-Z ablator. Adjacent quartz and polystyrene samples (2 mm × 1 mm × 0.2 mm thick) were glued to the back of the quartz baseplate using an ultralow viscosity UV-cured epoxy that produced glue layers <2 μm thick. For the laser intensities used, simulations using the radiation hydrodynamics code LILAC [32] indicate that x rays produced by the laser plasma would be absorbed within the quartz baseplate with a negligible level of preheat reaching the samples on the back [33]. The quartz and CH samples had initial densities of 2.65 and 1.05 g/cm^3, respectively. Density uncertainties were quoted to be 1% from the supplier.

Shock velocities were measured using a line-imaging velocity interferometer system for any reflector (VISAR) [34,35]. The VISAR measures the phase change produced by Doppler-shifted light reflecting off the shock front in the samples. Experiments were performed at pressures above where the shock had melted both materials and formed a reflecting front. This corresponds to ~150 GPa in quartz [36] and ~80 GPa in CH [17]. A 965-Å single layer MgF$_2$ antireflective coating for 532 nm was applied to the back surface of the target to minimize ghost reflections from the sample-vacuum interface. The raw VISAR data [Fig. 1(b)] was analyzed using the Fourier transform method to determine the phase [37]. To account for 2π ambiguities in phase, two VISARs were with different velocity sensitivities were used. The free-space
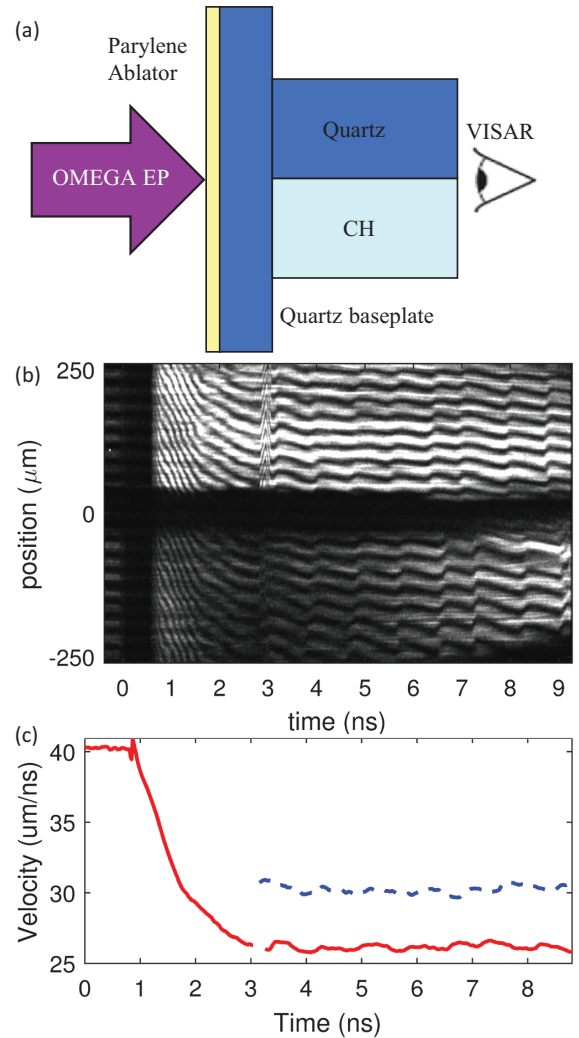
FIG. 1. (a) Schematic of multilayered flat targets consisting of Parylene-N ablator, quartz baseplate, and quartz and CH samples. (b) The raw VISAR data from shot 22092 shows a decaying shock in the quartz baseplate followed by a perturbed steady shock in the quartz and CH samples. (c) The perturbations to the quartz (red) and CH (dashed blue) shock velocities shown were used to determine the CH sound velocity. The data were averaged over four fringes (~100 μm) in the center of the target [±50–150 μm in (b)].

sensitivities used were 2.74 and 6.76 km/s/fringe, which correspond to velocity sensitivities of 1.72 and 4.25 km/s/fringe in polystyrene and 1.76 and 4.37 km/s/fringe in quartz. Uncertainty in the velocity was ~3% of a fringe, which resulted in <1% uncertainties due to multiple fringe jumps. The streak cameras for the two VISARs used 9- and 15-ns sweep durations, resulting in temporal sensitivities of ~30 and ~50 ps. A sample of an extracted shock velocity profile is given in Fig. 1(c).

III. QMD CALCULATIONS

The QMD calculations have been performed by using the Vienna *Ab-initio* Simulation Package (VASP) [38,39], which is based on the finite-temperature density functional theory (FTDFT). Here the electrons are treated

quantum mechanically by plane-wave FTDFT calculations using the Perdew-Burke-Ernzerhof (PBE) exchange-correlation functional [40,41] in the generalized gradient approximation (GGA). The electron-ion interaction is modeled by a projector-augmented wave (PAW) pseudopotential [42]. The system was assumed to be in local thermodynamic equilibrium with equal electron and ion temperatures ($T_e = T_i$). The ion temperature was kept constant by the Nosé-Hoover thermostat during a molecular-dynamics simulation.

A periodically replicated cubic cell is used with equal numbers of C and H atoms. The plasma density and the number of atoms determine the volume of the cell. We used a total of 125-C and 125-H atoms. For each molecular dynamics (MD) step, a set of electronic-state functions for each k point is self-consistently determined for an ionic configuration. Under the Born-Oppenheimer approximation, the ions are moved classically with a velocity Verlet algorithm, according to the combined ionic and electronic forces. Repeating the two steps propagates the system in time, resulting in a set of self-consistent ion configurations and electronic-state functions. EOS quantities of pressure and internal energy can be directly outputted from such QMD calculations.

We employed the Γ-point sampling of the first Brillouin zone in the cubic cell. To converge the EOS calculations, we set the plane-wave cutoff energy to $E_{max} = 1000\,\text{eV}$ and adopted the PAW potentials with hard cores (core radii of 1.1 and 0.8 atomic units for C and H, respectively). Four active electrons ($2s2p$) were used for C in the simulations. A large number of energy bands (up to $N_b = 6000$) have been included to ensure that the population of the highest energy band is $<10^{-5}$. For the lowest temperature, we used 500 bands and a time step of $\Delta t = 0.5\,\text{fs}$, while at the highest temperature, we employed a larger number of bands (11 000) and a small time step of $\Delta t = 0.011\,\text{fs}$. We calculated EOS on a density and temperature grid, from which we derived the Hugoniot. For sound velocity and Grüneisen parameter calculations, we first fit the principal Hugoniot's pressure P and internal energy E as a function of density ρ by a polynomial. We tested the applicability of the PAW pseudopotentials for the shock Hugoniot conditions studied here similar to previously reported methods [43,44]. Additional details can be found in Ref. [18].

IV. ANALYSIS

A. Hugoniot

The CH Hugoniot was determined using the impedance matching (IM) technique referenced to the quartz baseplate. As both quartz and CH are transparent to the 532-nm VISAR laser, the shock velocity was measured *in situ*, and a zeroth-order correction could be used to account for the shock transit across the glue layer. The Hugoniot and release of the quartz standard were calculated using the updated model from Desjarlais, Knudson, and Cochrane [45,46]. The model uses a Mie-Grüneisen EOS with a pressure-dependent U_S-u_p relation and Γ_{eff}, where U_S is the shock velocity, u_p is the particle velocity, and Γ_{eff} is the effective Grüneisen parameter. The shock pressure P, density ρ, and energy E are determined

from the Rankine-Hugoniot relations [47]:

$$\rho = \frac{\rho_0 U_S}{U_S - u_p}, \qquad (1)$$

$$P = \rho_0 U_S u_p, \qquad (2)$$

$$E = E_0 + \frac{1}{2}(P + P_0)\left(\frac{1}{\rho_0} - \frac{1}{\rho}\right), \qquad (3)$$

where the subscript 0 denotes the ambient condition. The release curve is determined by calculating the isentrope that intersects the given quartz Hugoniot state. The CH pressure and particle velocity was determined by finding the intersection of the quartz release and the CH $P - u_p$ Hugoniot given in Eq. (2).

B. Sound velocity

The sound velocity was measured using an unsteady wave analysis [48] with the profile matching technique described in Ref. [33] for pressures ranging from 100 to 850 GPa. The shock pressure and density were assumed to remain approximately constant at values described in the previous section. Over the duration of the laser pulse, the steady shock fronts in both the quartz and CH samples were overtaken by a series of unsupported waves generated by reverberations of the ablator between the ablation front and quartz baseplate. Similar to Ref. [33] a linear fit was subtracted from the CH and quartz shock velocities and the resulting profiles of δU_s vs t in the CH and quartz were matched by modifying the quartz profile using

$$\delta U_S^{CH}\left(t - t_0^{CH}\right) = G\delta U_S^Q\left[F\left(t - t_0^Q\right) + \delta t_0\right] + \delta u_0, \qquad (4)$$

where F and G are scale factors for the temporal spacing and amplitude of perturbations, t_0 is the time where the shock breaks out into the CH sample and quartz witness, and δt_0 and δu_0 provide small corrections to match the first perturbation and average value after subtraction of the linear fit. Both legs of the VISAR system were fit independently and the F parameters were compared to determine the uncertainty in the matching. This produced a fitting uncertainty of 2–3%.

The F values were used to determine the sound velocity by relating the Mach number of acoustic waves in the CH to those for the shocked and released quartz. Acoustic waves propagating on the quartz side of the target encounter the interfaces between the quartz baseplate, epoxy, and quartz sample. Simulations carried out using the hydrocode CTH [49] identified that for the glue thickness present in these experiments, the effects from the epoxy EOS are negligible due to the arrival time of the perturbations in the sample. Hence, the only feature that needs to be considered is the receding shock front, which increases the time between subsequent waves by a factor of $\frac{1}{1-M_Q}$, where $M_Q < 1$ is the Mach number of the acoustic waves in the shocked quartz fluid.

On the CH side of the target, acoustic waves propagate through the quartz baseplate and thin epoxy layer prior to entering the sample overtaking the shock front there. Similar to the quartz side of the target, the epoxy was ignored as any impacts would occur prior to the transit of the first perturbation. Remaining features that required consideration

were the release in the quartz, the density jump at the material interface, and the receding shock front in the CH. Since the analysis was conducted in the Lagrangian frame, the material interface is stationary and doesn't affect the temporal spacing of perturbations. Across the release wave, changes to the pressure, density, and local sound velocity affect the acoustic wave propagation by $\frac{1+M_d}{1+M_u}$, where u and d denote the regions upstream and downstream of the release, respectively. The Mach number in the CH, M_{CH}, can be determined from the F parameter and the transit factors for shock and release waves as

$$M_{CH} = 1 - \frac{(1 - M_Q)(1 + M_d)}{F(1 + M_u)}. \qquad (5)$$

The sound velocity of shocked polystyrene, C_S, is then determined from the Hugoniot and Mach number:

$$C_S = \frac{\Delta P}{\Delta u_p \rho M}, \qquad (6)$$

where ΔP and Δu_p are the change in pressure and particle velocity across the shock front, respectively.

V. RESULTS AND DISCUSSION

A. Hugoniot

Twenty-five new data points further constrain the polystyrene Hugoniot for pressures ranging from 100 to 1040 GPa and are given in Fig. 2 and Table I. These results (yellow diamonds) are in good agreement with the experimental results from Barrios *et al.* [17] (blue squares) after reanalysis using the updated quartz model from Desjarlais, Knudson, and Cochrane [45]. Additionally, these results agree well with the FPEOS-0516 Hugoniot based on QMD calculations by Hu, Boehly, and Collins [27] (dashed-double-dotted black line) over the range of pressure where the data overlap. When comparing to theoretical results, it is valuable to note that the uncertainty in these results is small enough to distinguish oscillation effects on the Hugoniot in quantum statistical calculations [50,51].

Comparing these results to EOS tables from the SESAME [52] (7593) and LEOS (5111 and 5400) libraries, we find that the SESAME 7593 table (dashed-dotted green line) best represents the experimental Hugoniot. This would be expected as the SESAME 7593 is the most recent polystyrene table and was constrained to the Barrios data [17], whereas LEOS 5111 (long-dashed blue line) is an older polystyrene table and LEOS 5400 [7] (dashed purple line) is a GDP table that has been scaled for the difference in density [5]. Over the pressure range studied, the LEOS 5111 table is significantly more compressible and falls outside a 2σ bound for most data above 200 GPa. Conversely, the LEOS 5400 table agrees well with data above ∼400 GPa but is systematically stiff at lower pressures. Construction of the SESAME 7593 table used Thomas-Fermi-Dirac electrons and Johnson ions with the cold curve and Hugoniot fitted to experimental data [5]. The LEOS 5111 and 5400 tables both use an HQEOS model with Purgatorio electron-thermal contribution [5].

An updated linear U_S-u_p relation was determined for polystyrene shocked into the liquid phase using these data as well as the reanalyzed results from Barrios *et al.* [17]. Fit and
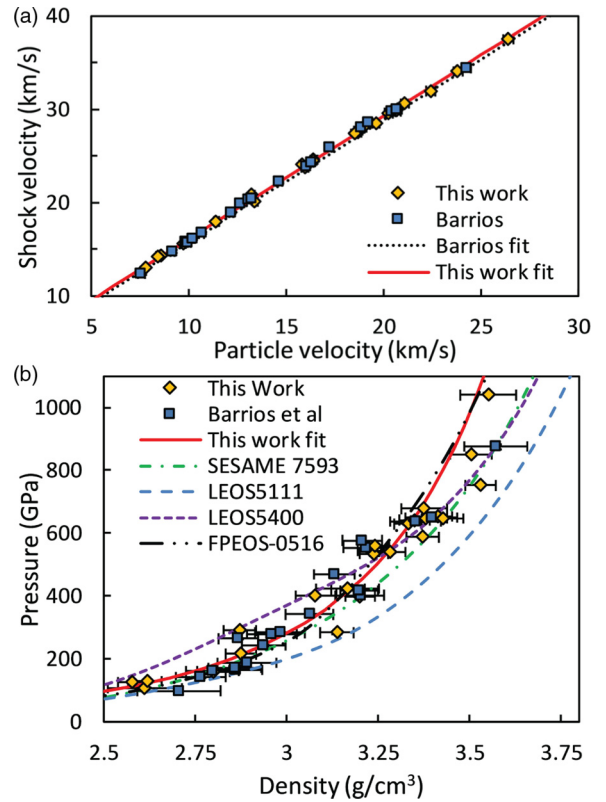
FIG. 2. (a) U_S-u_p results from this work (yellow diamonds) are in good agreement with reanalyzed results from Barrios (blue squares). The new U_S-u_p fit (solid red line) is systematically stiffer than the fit determined by Barrios (dotted black line) using an earlier version of the quartz standard. (b) The experimental results are in good agreement with QMD-based FPEOS-0516 (dashed-double-dotted black line) and the SESAME 7593 (dashed-dotted green line) EOS tables. Neither LEOS 5111 (long-dashed blue line) nor 5400 (dashed purple line) are in good agreement with the data, with LEOS 5111 being too compressible and LEOS 5400 being too incompressible at pressures below 400 GPa.

covariance parameters are given in Table II. The updated fit exhibits a stiffer behavior than the SESAME and LEOS tables, but is in excellent agreement with FPEOS-0516 which was based on QMD calculations. This fit can be used to accurately model the behavior of CH for pressures up 2000 GPa. At pressures greater than 5000 GPa, QMD calculations imply that a linear U_S-u_p relation does not fully capture the dynamic behavior of polystyrene, and the results from Hu *et al.* may better represent the CH Hugoniot [22,27].

B. Sound speed

The sound velocity data determined from the unsteady wave analysis constrain the bulk modulus and acoustic properties of liquid CH in the ICF relevant regime. The data exhibit a monotonic increase in acoustic wave velocity with increasing pressure, with an apparent change in slope between 300 and 500 GPa (Fig. 3). The QMD results (black circles) agree well with the experimental data and exhibit a slight plateau in sound velocity in the 400–500-GPa range; this plateau is likely due to an electronic transition upon completion of

TABLE I. Hugoniot and sound velocity measurements for CH. U_S^Q and U_S^{CH} are the shock velocities for quartz and CH, respectively; all other quantities listed are for the shocked CH (u_p values have been rounded to two decimal places after calculation of P and ρ). Subscripts 1 and 2 denote which VISAR was used to determine the given F value. The uncertainty in F was estimated by averaging the two values for each shot and found to be 2–3%.

Shot	U_S^Q (km/s)	U_S^{CH} (km/s)	u_p (km/s)	P (GPa)	ρ (g/cm^3)	F_1	F_2	C_S (km/s)	Γ
19920	12.05 ± 0.20	13.01 ± 0.07	7.78 ± 0.19	106.3 ± 2.7	2.61 ± 0.10	1.09	1.00	13.08 ± 0.94	0.47 ± 0.24
21316	12.89 ± 0.07	14.23 ± 0.07	8.43 ± 0.07	126.0 ± 1.2	2.58 ± 0.04	1.08	1.02	14.27 ± 0.79	0.21 ± 0.18
21314	13.04 ± 0.07	14.31 ± 0.07	8.57 ± 0.07	128.8 ± 1.2	2.62 ± 0.04	1.09	1.05	13.74 ± 0.60	0.40 ± 0.13
19915	14.38 ± 0.07	15.61 ± 0.07	9.76 ± 0.07	159.9 ± 1.3	2.80 ± 0.04	1.02	1.06	14.82 ± 0.70	0.58 ± 0.09
19914	16.27 ± 0.07	17.99 ± 0.07	11.42 ± 0.08	215.7 ± 1.6	2.88 ± 0.04	1.02	1.00	16.90 ± 0.74	0.49 ± 0.10
19921	18.34 ± 0.07	20.13 ± 0.07	13.39 ± 0.08	283.1 ± 1.9	3.14 ± 0.05	0.97	1.01	17.53 ± 1.01	0.69 ± 0.06
19922	18.30 ± 0.07	20.86 ± 0.11	13.23 ± 0.08	289.8 ± 2.1	2.87 ± 0.04	1.02	1.03	18.44 ± 0.73	0.37 ± 0.12
17868	21.08 ± 0.07	23.76 ± 0.07	15.97 ± 0.08	398.3 ± 2.3	3.20 ± 0.04	1.03	1.03	18.81 ± 0.68	0.69 ± 0.04
19912	21.02 ± 0.07	24.05 ± 0.14	15.85 ± 0.08	400.2 ± 2.8	3.08 ± 0.05	1.03	1.04	19.52 ± 0.73	0.54 ± 0.08
16769	21.55 ± 0.07	24.52 ± 0.10	16.39 ± 0.09	422.0 ± 2.6	3.17 ± 0.04	1.13	1.17	17.15 ± 0.60	0.74 ± 0.04
17859	21.59 ± 0.18	24.58 ± 0.08	16.43 ± 0.21	424.0 ± 5.6	3.17 ± 0.09	1.07	1.14	18.00 ± 0.89	0.73 ± 0.07
22089	23.75 ± 0.07	27.41 ± 0.07	18.53 ± 0.09	533.2 ± 2.7	3.24 ± 0.04	1.08	0.99	21.69 ± 1.63	0.60 ± 0.07
17861	23.90 ± 0.07	27.48 ± 0.07	18.69 ± 0.09	539.4 ± 2.8	3.28 ± 0.04	0.97	1.09	21.88 ± 1.90	0.63 ± 0.07
17870	23.94 ± 0.07	27.71 ± 0.07	18.70 ± 0.09	544.2 ± 2.8	3.23 ± 0.04	1.13	1.13	19.55 ± 0.54	0.70 ± 0.03
22097	24.19 ± 0.07	28.03 ± 0.07	18.95 ± 0.09	557.7 ± 2.8	3.24 ± 0.04	1.07	1.05	21.37 ± 0.98	0.61 ± 0.05
22090	24.81 ± 0.08	28.49 ± 0.07	19.62 ± 0.10	586.9 ± 3.2	3.37 ± 0.04	1.01	1.02	22.45 ± 1.10	0.68 ± 0.04
17863	25.49 ± 0.07	29.58 ± 0.07	20.26 ± 0.09	629.2 ± 3.1	3.33 ± 0.04	1.08	1.10	21.44 ± 0.72	0.68 ± 0.03
22091	25.71 ± 0.07	29.83 ± 0.09	20.48 ± 0.09	641.4 ± 3.2	3.35 ± 0.04	1.04	1.06	22.75 ± 1.09	0.68 ± 0.04
16767	25.82 ± 0.12	29.89 ± 0.07	20.61 ± 0.15	646.8 ± 4.9	3.38 ± 0.06	1.05	1.08	22.20 ± 0.81	0.68 ± 0.04
22098	25.87 ± 0.11	29.81 ± 0.07	20.68 ± 0.14	647.2 ± 4.5	3.43 ± 0.06	1.11	1.08	20.94 ± 0.92	0.74 ± 0.03
19908	25.94 ± 0.07	29.96 ± 0.07	20.74 ± 0.09	652.5 ± 3.1	3.41 ± 0.04	1.03	0.99	23.82 ± 1.06	0.65 ± 0.04
22092	26.32 ± 0.13	30.61 ± 0.08	21.09 ± 0.16	677.7 ± 5.4	3.38 ± 0.06	1.08	1.11	21.81 ± 0.93	0.68 ± 0.04
22095	27.61 ± 0.07	31.93 ± 0.07	22.43 ± 0.10	752.1 ± 3.5	3.53 ± 0.04	1.07	1.08	22.65 ± 1.04	0.75 ± 0.02
22100	29.05 ± 0.09	34.03 ± 0.12	23.83 ± 0.13	851.6 ± 5.1	3.50 ± 0.08	1.09	1.09	23.92 ± 1.10	0.70 ± 0.03
22099	31.63 ± 0.13	37.49 ± 0.14	26.41 ± 0.20	1039.4 ± 8.3	3.55 ± 0.08				

dissociation. Below 300 GPa, the level of agreement decreases, which may indicate a difference from predicted behavior in the dissociation regime.

Above 300 GPa, QMD, SESAME 7593, and LEOS 5111 predict similar sound velocities as a function of the shock pressure and are consistent with (but slightly lower than) our data. Over this range, LEOS 5400 underpredicts the sound velocity and exhibits distinctly different pressure dependence. Below 300 GPa, all four models have similar values and slopes in the $C_S - P$ plane, but again are somewhat lower than our data. The experimental and QMD results agree best with the SESAME 7593 table for pressures above 170 GPa. Below 170 GPa, the experimental data still agree with the SESAME 7593 table, however the QMD results are in better agreement with LEOS 5111. The LEOS 5400 table has poor agreement with the experimental data and QMD results for pressures above 250 GPa. The tables converge for pressures exceeding the range of these experiments, such that sound velocities in

the LEOS 5400 table may be valid for pressures in excess of 1000 GPa.

C. Grüneisen parameter

The Grüneisen parameter Γ of liquid CH was determined from the measured Hugoniot and sound velocity using the method described by McQueen [6]. This method uses the derivative along the Hugoniot, $(\frac{dP}{dV})_H$, and the sound velocity, $C_S = (\frac{dP}{dV})_S$, to define vectors on the thermodynamic (P, V, E) plane from which to calculate $\Gamma = \frac{1}{V}(\frac{dP}{dE})_V$.

For densities greater 3.1 g/cm^3 (corresponding to pressures >350 GPa), the Grüneisen parameter Γ is approximately constant ($\Gamma = 0.68 \pm 0.04$) close to the theoretical prediction for an ideal gas ($\Gamma \approx 0.66$) at high temperatures (Fig. 4). Previous work indicated that at this condition, the reflectivity of the shock front reaches a constant value, indicating that dissociation is complete, and the material is an atomic fluid [17,18]. Approaching the asymptotic limit for an ideal gas at pressures near the completion of dissociation has also been demonstrated for fused silica [33] and MgO [53]. This indicates there may be a region in phase-space where the mechanical properties of a dense atomic fluid can be treated classically with an ideal gas model rather than the more complex Thomas-Fermi model [54]. At higher pressures and temperatures (e.g., Gbar EOS), more complex models

TABLE II. Fit and covariance matrix parameters for liquid CH Hugoniot of form $U_S = C_0 + S u_p$ (U_S and u_p in km/s).

C_0 (km/s)	S	$\sigma_{C_0}^2(\times 10^{-3})$	$\sigma_S^2(\times 10^{-5})$	$\sigma_{C_0}\sigma_S(\times 10^{-4})$
2.991	1.311	8.089	3.178	-4.848
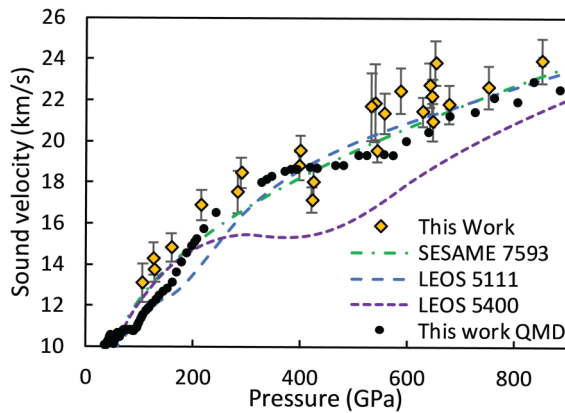
FIG. 3. The isentropic sound velocity measurements (yellow diamonds) are in good agreement with QMD calculations (black circles) of the sound velocity along the Hugoniot. Both sets of data show a slight plateau in sound velocity between 400 and 500 GPa. The results also agree well with the SESAME 7593 (dashed-dotted green line) table, as well as LEOS 5111 (long-dashed blue line) for pressures >350 GPa and LEOS 5400 (dashed purple line) at low pressure. The large plateau in sound velocity exhibited in LEOS 5400 is not supported by these results, such that LEOS 5400 underpredicts the sound velocity above 200 GPa.

become necessary due to ionization of core electrons and the associated need to treat electrons quantum mechanically [55].

For densities below $3.1 \, \mathrm{g/cm^3}$, the experimentally determined Grüneisen parameter increases with density and is in good agreement with our QMD results as well as the GDP results by Colin-Lalu *et al.* (gray connected squares) [19]. Both QMD results indicate that Γ reaches an approximately
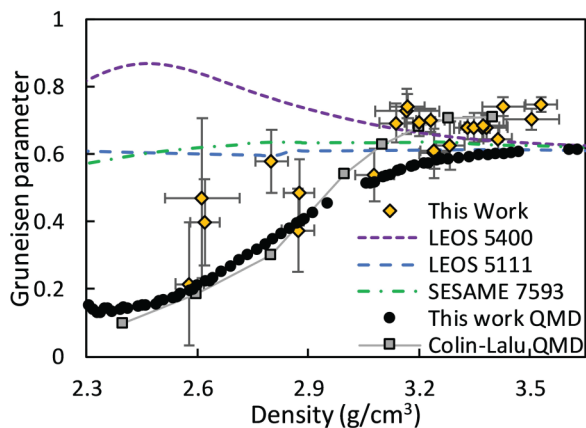
FIG. 4. Lines and symbols same as in Fig. 3. Measurements of the polystyrene Grüneisen parameter exhibit an increase with density until reaching an approximately constant value at $\sim 3.2 \, \mathrm{g/cm^3}$. This behavior is in good agreement with these QMD calculations for CH and previous calculations for GDP (connected gray squares). None of the EOS tables shown agree with these results and the SESAME 7593 table is the only one where the Grüneisen parameter increases with density before reaching a nearly constant result. The LEOS 5111 table has an approximately constant Grüneisen parameter for the entire density range shown. The LEOS 5400 table exhibits behavior opposite the experimental and QMD results albeit with the maximum deviation from the asymptotic value being similar.

constant value (albeit different values) at $\sim 3.3 \, \mathrm{g/cm^3}$. The Colin-Lalu results better agree with our data. Despite the uncertainties in the data, the data exhibit a change to a reduced or negligible slope at $\sim 3.1 \, \mathrm{g/cm^3}$ suggesting that dissociation is complete. When considering the pressure, this corresponds to ~ 350 GPa, which is 50–100 GPa greater than where Barrios *et al.* observed a saturation in reflectivity [17], which indicates completion of dissociation [56]. We note that the reflectivity uncertainty in the Barrios data is large and values above 350 GPa are $\sim 10\%$ greater than those in the range 250–300 GPa, so the true saturation may occur closer to 350 GPa, which agrees well with our result. At lower densities, Γ increases as dissociation is occurring; this differs from other materials where liquid Grüneisen parameters have been measured and found to monotonically decrease through the dissociation regime [33,53]. However, the increase in Γ as dissociation is occurring was also identified in liquid D_2 [57], which indicates that it may be related to the presence of hydrogen. Further study on other plastics or hydrogen-rich compounds (such as water or methane) would be interesting to examine if this behavior persists.

Comparing these data and QMD results to EOS tables reinforces the need to correctly account for dissociation to accurately model the $P - E$ response of a material. The SESAME 7593 and LEOS 5400 tables both include dissociation using the method described by Young and Corey and show a change in Γ as the density changes [58]. This method assumes perfect dissociation into a mixed ideal gas and calculates the fraction of atoms that are bound as molecules and separated into an atomic gas. However, the method does not allow for dissociation into different molecules as an intermediate state, such as the case where the benzene rings are freed from the CH structure [59]. Additionally, the method requires empirical data for the density dependence of the dissociation energy, which is not adequately constrained. The LEOS 5111 table has a nearly constant Γ over the entire range of densities shown, which indicates that it likely does not account for any thermomechanical effects due to dissociation. Conversely, the QMD calculations directly determine Γ from the phonon spectrum and imparts an explicit density dependence to form a new EOS [19].

None of the tables correctly model how dissociation affects the mechanical behavior of high-pressure CH. The only table that exhibits Γ increasing with density is SESAME 7593, but that table reaches a constant value at $\sim 2.7 \, \mathrm{g/cm^3}$ (vs $\sim 3.1 \, \mathrm{g/cm^3}$ in our data), and has a minimum value of ~ 0.5. QMD simulations and experimental data imply that Γ should be < 0.2 for conditions above shock-melting but below the onset of dissociation. This large difference can have a significant impact on the off-Hugoniot behavior of a material. The LEOS 5400 table exhibits the opposite behavior of the QMD calculations and experimental results. In the table, Γ increases to a peak value of ~ 0.9 at $2.4 \, \mathrm{g/cm^3}$. This value is six times that which is predicted by QMD and indicates that the table does not model the impact of dissociation upon the mechanical properties correctly. This is likely due to the table being built using calculations for the atomic fluid with dissociation added rather than QMD calculations of Γ. The LEOS 5400 table includes fitting of the release curve to impedance matching data for GDP releasing into D_2 [7], however the

discrepancy between the tabular Hugoniot and experimental data, identified in Sec. V A), indicates that the correct release state was achieved by incorrectly modeling both the Hugoniot and release.

D. Application to ICF experiments

Modeling of ICF experiments depends on precise knowledge of the ablator and fuel EOS. Because the capsule implosion is driven by a series of shocks with increasing strength, the propagation of subsequent shocks will depend on the conditions of the precompressed fluid ahead of the shock. These conditions, being off the principal Hugoniot, require accurate knowledge of the Grüneisen parameter in the compressed medium. Colin-Lalu *et al.* showed that choosing a poor EOS that doesn't properly match the Hugoniot and Grüneisen parameter of a GDP ablator can result in the coalescence of the first and second shocks occurring ∼600 ps earlier than desired, whereas the tolerance is 50–100 ps [19]. As all three EOS tables shown do not accurately represent the Hugoniot and Grüneisen parameter, their use in designing an ICF implosion would negatively impact the experiment by changing the subsequent-shock pressure and density such that shock coalescence may no longer occur at either the desired target depth or with the desired pressure in the fuel.

In addition to mistiming shock coalescence in the fuel, the use of an inaccurate EOS can have a significant impact on the growth of hydrodynamic instabilities which can result in the injection of cold material into the hot spot and failure to reach ignition. In ICF experiments using plastic ablators, the first shock is typically 100–300 GPa in the ablator [2,10,19]. Over this range of pressures, the sound velocity increases from 13 to 17.5 km/s, however in the LEOS 5400 table, the sound velocity plateaus at ∼15.5 km/s from 200 to 400 GPa. This discrepancy in the sound velocity impacts the growth rate η and oscillatory behavior of the RM instability, which can be given as

$$\eta = \eta_0 \frac{\sin kC_S t}{kC_S t}, \tag{7}$$

where $k = \frac{L}{R}$ and L and R are the Legendre mode and radius of an ICF capsule, respectively. η_0 is the initial growth factor for the first shock [9]. The use of an incorrect sound velocity changes the magnitude of the growth factor by ∼15%, and shifts the Legendre mode with zero growth for a nominal pulse from $L \approx 70$ to $L \approx 60$ [10]. This increases the number of modes with negative growth which invert and grow into the capsule during the acceleration phase, thereby degrading the implosion symmetry relative to the design simulations [10]. To mitigate the increased instability growth, the timing between shocks needs to be shortened, which requires stronger shocks that will raise the fuel adiabat and limit possible compression. New designs to balance increased instability growth with an increased fuel adiabat are required to optimize capsule performance for future experiments.

VI. CONCLUSION

The principal Hugoniot, sound velocity, and Grüneisen parameter of polystyrene were measured for pressures from 100 to 1000 GPa using laser-driven shocks on the OMEGA EP laser facility. These data, added to existing results, further constrain the principal Hugoniot at pressures relevant to the initial stages of an ICF implosion. The sound velocity was found to increase from 13 km/s at 100 GPa to 24 km/s at 850 GPa and is in good agreement with QMD calculations and the SESAME 7593 table. The Grüneisen parameter was found to increase with density above melt and approach a constant value of ∼0.7 at densities above 3.1 g/cm^3. This behavior is in good agreement with QMD calculations presented here and in previous work. No tabular EOS models accurately predict the change in the Grüneisen parameter at densities below 3.1 g/cm^3.

The most recent EOS table for GDP, LEOS 5400, poorly represents the sound velocity and Grüneisen parameter over the pressure range relevant to the first shock in an ICF experiment. This discrepancy is sufficient to impact timing of shock coalescence and the seed perturbations created by the Richtmyer-Meshkov instability enough to prevent a target from forming a uniform central hot spot. Development of a new table which accurately represents the off-Hugoniot properties is necessary for design and modeling of future ICF experiments using plastic ablators.

[1] R. Betti and O. A. Hurricane, Nat. Phys. **12**, 435 (2016).

[2] S. Haan, J. Lindl, D. Callahan, D. Clark, J. Salmonson, B. Hammel, L. Atherton, R. Cook, M. Edwards, and S. Glenzer, Phys. Plasmas **18**, 051001 (2011).

[3] T. R. Boehly, V. N. Goncharov, W. Seka, M. A. Barrios, P. M. Celliers, D. G. Hicks, G. W. Collins, S. X. Hu, J. A.

Marozas, and D. D. Meyerhofer, Phys. Rev. Lett. **106**, 195005 (2011).

[4] T. R. Boehly, D. H. Munro, P. M. Celliers, R. E. Olson, D. G. Hicks, V. N. Goncharov, G. W. Collins, H. F. Robey, S. X. Hu, J. A. Marozas, T. C. Sangster, O. L. Landen, and D. D. Meyerhofer, Phys. Plasmas **16**, 056302 (2009).

[5] J. A. Gaffney, S. X. Hu, P. Arnault, A. Becker, L. X. Benedict, T. R. Boehly, P. M. Celliers, D. M. Ceperley, O. Čertík, J. Clérouin, G. W. Collins, L. A. Collins, J. F. Danel, N. Desbiens, M. W. C. Dharma-wardana, Y. H. Ding, A. Fernandez-Pañella, M. C. Gregor, P. E. Grabowski, S. Hamel *et al.*, High Energy Density Physics **28**, 7 (2018).

[6] R. G. McQueen, in *Proceedings of the 20th American Physical Society Topical Conference on Shock Compression of Condensed Matter*, edited by S. C. Schmidt, R. D. Dick, J. W. Forbes, and D. G. Tasker (Elsevier, Williamsburg, VA, 1991), p. 75.

[7] S. Hamel, L. X. Benedict, P. M. Celliers, M. A. Barrios, T. R. Boehly, G. W. Collins, T. Döppner, J. H. Eggert, D. R. Farley, D. G. Hicks, J. L. Kline, A. Lazicki, S. LePape, A. J. Mackinnon, J. D. Moody, H. F. Robey, E. Schwegler, and P. A. Sterne, Phys. Rev. B **86**, 094113 (2012).

[8] V. N. Goncharov, Phys. Rev. Lett. **82**, 2091 (1999).

[9] V. N. Goncharov, O. V. Gotchev, E. Vianello, T. R. Boehly, J. P. Knauer, P. W. McKenty, P. B. Radha, S. P. Regan, T. C. Sangster, and S. Skupsky, Phys. Plasmas **13**, 012702 (2006).

[10] J. L. Peterson, D. S. Clark, L. P. Masse, and L. J. Suter, Phys. Plasmas **21**, 092710 (2014).

[11] S. Regan, R. Epstein, B. Hammel, L. Suter, J. Ralph, H. Scott, M. Barrios, D. Bradley, D. Callahan, and C. Cerjan, Phys. Plasmas **19**, 056307 (2012).

[12] T. Ma, P. Patel, N. Izumi, P. Springer, M. Key, L. Atherton, L. Benedetti, D. Bradley, D. Callahan, and P. Celliers, Phys. Rev. Lett. **111**, 085004 (2013).

[13] M. A. Barrios, T. R. Boehly, D. G. Hicks, D. E. Fratanduono, J. H. Eggert, G. W. Collins, and D. D. Meyerhofer, J. Appl. Phys. **111**, 093515 (2012).

[14] A. J. MacKinnon, N. B. Meezan, J. S. Ross, S. L. Pape, L. B. Hopkins, L. Divol, D. Ho, J. Milovich, A. Pak, J. Ralph, T. Döppner, P. K. Patel, C. Thomas, R. Tommasini, S. Haan, A. G. MacPhee, J. McNaney, J. Caggiano, R. Hatarik, R. Bionta *et al.*, Phys. Plasmas **21**, 056318 (2014).

[15] A. N. Simakov, D. C. Wilson, S. A. Yi, J. L. Kline, D. S. Clark, J. L. Milovich, J. D. Salmonson, and S. H. Batha, Phys. Plasmas **21**, 022701 (2014).

[16] D. R. Harding, M. J. Bonino, W. Sweet, M. Schoff, A. Greenwood, N. Satoh, M. Takagi, and A. Nikroo, Matter Radiat. Extremes **3**, 312 (2018).

[17] M. A. Barrios, D. G. Hicks, T. R. Boehly, D. E. Fratanduono, J. H. Eggert, P. M. Celliers, G. W. Collins, and D. D. Meyerhofer, Phys. Plasmas **17**, 056307 (2010).

[18] S. X. Hu, L. A. Collins, V. N. Goncharov, J. D. Kress, R. L. McCrory, and S. Skupsky, Phys. Rev. E **92**, 043104 (2015).

[19] P. Colin-Lalu, V. Recoules, G. Salin, T. Plisson, E. Brambrink, T. Vinci, R. Bolis, and G. Huser, Phys. Rev. E **94**, 023204 (2016).

[20] N. Ozaki, T. Ono, K. Takamatsu, K. Tanaka, M. Nakano, T. Kataoka, M. Yoshida, K. Wakabayashi, M. Nakai, and K. Nagai, Phys. Plasmas **12**, 124503 (2005).

[21] A. V. Bushman, I. V. Lomonosov, V. E. Fortov, K. V. Khishchenko, M. V. Zhernokletov, and Y. N. Sutulov, JETP Lett. **82**, 895 (1996).

[22] T. Döppner, D. C. Swift, A. L. Kritcher, B. Bachmann, G. W. Collins, D. A. Chapman, J. Hawreliak, D. Kraus, J. Nilsen, S. Rothman, L. X. Benedict, E. Dewald, D. E. Fratanduono, J. A. Gaffney, S. H. Glenzer, S. Hamel, O. L. Landen, H. J. Lee, S. LePape, T. Ma *et al.*, Phys. Rev. Lett. **121**, 025001 (2018).

[23] S. Root, T. R. Mattsson, K. Cochrane, R. W. Lemke, and M. D. Knudson, J. Appl. Phys. **118**, 205901 (2015).

[24] M. C. Akin, D. E. Fratanduono, and R. Chau, J. Appl. Phys. **119**, 045901 (2016).

[25] G. Huser, V. Recoules, N. Ozaki, T. Sano, Y. Sakawa, G. Salin, B. Albertazzi, K. Miyanishi, and R. Kodama, Phys. Rev. E **92**, 063108 (2015).

[26] G. Huser, N. Ozaki, P. Colin-Lalu, V. Recoules, T. Sano, Y. Sakawa, K. Miyanishi, and R. Kodama, Phys. Plasmas **25**, 052706 (2018).

[27] S. X. Hu, T. R. Boehly, and L. A. Collins, Phys. Rev. E **89**, 063104 (2014).

[28] K. V. Khishchenko, V. E. Fortov, and I. V. Lomonosov, Int. J. Thermophys. **23**, 211 (2002).

[29] X. Zhang, G. Wang, B. Luo, F. Tan, S. N. Bland, J. Zhao, C. Sun, and C. Liu, J. Mater. Sci. **53**, 12628 (2018).

[30] L. J. Waxer, D. N. Maywar, J. H. Kelly, T. J. Kessler, B. E. Kruschwitz, S. J. Loucks, R. L. McCrory, D. D. Meyerhofer, S. F. B. Morse, C. Stoeckl, and J. D. Zuegel, Opt. Photonics News **16**, 30 (2005).

[31] Y. Lin, G. N. Lawrence, and T. J. Kessler, Opt. Lett. **20**, 764 (1995).

[32] J. Delettrez, R. Epstein, M. C. Richardson, P. A. Jaanimagi, and B. L. Henke, Phys. Rev. A **36**, 3926 (1987).

[33] C. A. McCoy, M. C. Gregor, D. N. Polsin, D. E. Fratanduono, P. M. Celliers, T. R. Boehly, and D. D. Meyerhofer, J. Appl. Phys. **120**, 235901 (2016).

[34] L. M. Barker and R. E. Hollenbach, J. Appl. Phys. **43**, 4669 (1972).

[35] P. M. Celliers, D. K. Bradley, G. W. Collins, D. G. Hicks, T. R. Boehly, and W. J. Armstrong, Rev. Sci. Instrum. **75**, 4916 (2004).

[36] J. A. Akins and T. J. Ahrens, Geophys. Res. Lett. **29**, 31-1 (2002).

[37] P. M. Celliers, G. W. Collins, L. B. Da Silva, D. M. Gold, and R. Cauble, Appl. Phys. Lett. **73**, 1320 (1998).

[38] G. Kresse and J. Hafner, Phys. Rev. B **47**, 558 (1993).

[39] G. Kresse and J. Hafner, Phys. Rev. B **49**, 14251 (1994).

[40] J. P. Perdew, K. Burke, and M. Ernzerhof, Phys. Rev. Lett. **77**, 3865 (1996).

[41] J. P. Perdew, K. Burke, and M. Ernzerhof, Phys. Rev. Lett. **78**, 1396(E) (1997).

[42] G. Kresse and J. Furthmüller, Phys. Rev. B **54**, 11169 (1996).

[43] P. R. Levashov, G. V. Sin'ko, N. A. Smirnov, D. V. Minakov, O. P. Shemyakin, and K. V. Khishchenko, J. Phys.: Condens. Matter **22**, 505501 (2010).

[44] G. V. Sin'ko, N. A. Smirnov, A. A. Ovechkin, P. R. Levashov, and K. V. Khishchenko, High Energy Density Phys. **9**, 309 (2013).

[45] M. P. Desjarlais, M. D. Knudson, and K. R. Cochrane, J. Appl. Phys. **122**, 035903 (2017).

[46] M. D. Knudson and M. P. Desjarlais, Phys. Rev. B **88**, 184107 (2013).

[47] Y. B. Zel'dovich and Y. P. Raizer, *Physics of Shock Waves and High-Temperature Hydrodynamic Phenomena*. (Dover, New York, 2002).

[48] D. E. Fratanduono, D. H. Munro, P. M. Celliers, and G. W. Collins, J. Appl. Phys. **116**, 033517 (2014).

[49] J. M. McGlaun, S. L. Thompson, and M. G. Elrick, Int. J. Impact Eng. **10**, 351 (1990).

[50] N. Y. Orlov, M. A. Kadatskiy, O. B. Denisov, and K. V. Khishchenko, Matter Radiat. Extremes **4**, 054403 (2019).

[51] M. A. Kadatskiy and K. V. Khishchenko, J. Phys.: Conf. Ser. **653**, 012079 (2015).

[52] S. P. Lyon and J. D. Johnson, Los Alamos National Laboratory Report No. LA-UR-92-3407, 1992.

[53] C. A. McCoy, M. C. Marshall, D. N. Polsin, D. E. Fratanduono, P. M. Celliers, D. D. Meyerhofer, and T. R. Boehly, Phys. Rev. B **100**, 014106 (2019).

[54] S. Eliezer, A. K. Ghatak, and H. Hora, *Fundamentals of Equations of State* (World Scientific, Singapore, 2005).

[55] C. E. Starrett and D. Saumon, Phys. Rev. E **87**, 013104 (2013).

[56] D. G. Hicks, T. R. Boehly, J. H. Eggert, J. E. Miller, P. M. Celliers, and G. W. Collins, Phys. Rev. Lett. **97**, 025502 (2006).

[57] D. E. Fratanduono, M. Millot, A. F. Pañella, P. A. Sterne, G. W. Collins, D. G. Hicks, J. H. Eggert, T. R. Boehly, and P. M. Celliers, Phys. Plasmas **26**, 012710 (2019).

[58] D. A. Young and E. M. Corey, J. Appl. Phys. **78**, 3748 (1995).

[59] J. E. Huheey, E. A. Keiter, and R. L. Keiter, *Inorganic Chemistry: Principles of Structure and Reactivity* (Pearson Education, Delhi, India, 2000).